Double-resonant nanostructured gold surface for multiplexed detection

Antonio Minopoli,[1,2] Emanuela Scardapane,[1] Bartolomeo Della Ventura,[1] Julian A. Tanner,[3] Andreas Offenhäusser,[2] Dirk Mayer,[2,] and Raffaele Velotta[1,]**

[1]Department of Physics "E. Pancini", University Federico II, Via Cintia 26, 80126 Naples, Italy.

[2]Institute of Biological Information Processing (IBI-3), Bioelectronics, Forschungszentrum Jülich, 52425 Jülich, Germany.

[3]School of Biomedical Sciences, University of Hong Kong, Hong Kong SAR, China.

KEYWORDS: nanoplasmonics, plasmon-enhanced fluorescence, photochemical immobilization technique, apta-immunosensor, malaria, gold nanoparticle array, block copolymer micelle nanolithography.

ABSTRACT: A novel double-resonant plasmonic substrate for fluorescence amplification in a chip-based apta-immunoassay is herein reported. The amplification mechanism relies on plasmon-enhanced fluorescence (PEF) effect. The substrate consists of an assembly of plasmon-coupled and plasmon-uncoupled gold nanoparticles (AuNPs) immobilized onto a glass slide. Plasmon-coupled AuNPs are hexagonally-arranged along branch patterns whose resonance lies in the red

band (~675 nm). Plasmon-uncoupled AuNPs are sprinkled onto the substrate and they exhibit a narrow resonance at 524 nm. Numerical simulations of the plasmonic response of the substrate through finite-difference time-domain (FDTD) method reveal the presence of electromagnetic hot spots mainly confined in the interparticle junctions. In order to realize a PEF-based device for potential multiplexing applications, the plasmon resonances are coupled with the emission peak of 5-carboxyfluorescein (5-FAM) fluorophore and with both the excitation and emission peaks of cyanine 5 (Cy5) fluorophore. The substrate is implemented in a malaria apta-immunoassay for detecting *Plasmodium falciparum* lactate dehydrogenase (*Pf*LDH) in human whole blood. Antibodies against *Plasmodium* biomarkers constitute the capture layer, whereas fluorescently-labelled aptamers recognizing *Pf*LDH are adopted as top layer. The fluorescence emitted by 5-FAM and Cy5 fluorophores are linearly correlated to the *Pf*LDH concentration over five decades. The limits of detection are 50 pM (1.6 ng/mL) with the 5-FAM probe and 260 fM (8.6 pg/mL) with the Cy5 probe . No sample preconcentration and complex pretreatments are required. Average fluorescence amplifications of 160 and 5200 are measured in the 5-FAM and Cy5 channel, respectively. These results are reasonably consistent with those worked out by FDTD simulations. The proposed approach is very attractive if implemented in multiwell-plate-based bioassays for both signal redundancy and simultaneous monitoring of different proteins at low concentrations in complex matrices paving the way for potential multiplexed and high-throughput analysis.

1. INTRODUCTION

In the last few years, plasmonic nanostructures are routinely used to amplify the signal in plasmon-enhanced fluorescence (PEF),[1] surface plasmon-coupled emission (SPCE),[2] surface-

enhanced Raman scattering (SERS),[3] and surface-enhanced infrared absorption (SEIRA) applications.[4] In particular, the fluorescence amplification is highly desirable in biosensing applications since high brightness is crucial when remarkable sensitivity is required, particularly in presence of interfering background arising from biological systems or complex matrices.[5] Although the mechanism behind the PEF is still not entirely understood,[6] in principle the fluorescence enhancement (FE) can be ascribable to the resonant coupling between the surface plasmon of the metal nanostructure and the nearby fluorophore, which can lead to both the excitation and emission amplification.[1] The particular mechanism strongly depends on the spectral overlap between the fluorophore and the plasmon extinction as well as on the fluorophore-nanostructure distance.[7,8] In general, if the plasmonic resonance overlaps the fluorophore excitation, the local modification of the electromagnetic field induced by the nanostructure results into an increase of the fluorophore excitation rate due to the Förster resonance energy transfer (FRET) mechanism. On the contrary, if the spectral overlap concerns the fluorophore emission, the nanostructure alters the radiative and non-radiative decay rates through the Purcell effect and, hence, the fluorescence lifetime and quantum yield. Actually, the nanostructure acts as a resonant cavity that amplifies the fluorescence emission on-resonance while quenches it off-resonance. This is due to the modification of the local density of states (LDOS) induced by the cavity.[9] In real cases, both FRET and Purcell effects usually take place leading to a strong quenching at a few nanometer fluorophore-nanostructure separation distance, a large FE in the range 5-30 nm (with an optimum at ~10 nm), and a weak coupling at longer distances.

Rough metal surfaces constitute one of the simplest tools to realize a fluorescence enhancer for biosensing applications since they generally offer high densities of randomly distributed electromagnetic hot spots on macroscopic areas. Additionally, employing sensing area with no

discontinuities provides the substrate with a multitude of anchoring sites for biomolecules so to make easier the bioreceptor-substrate binding. Nevertheless, their moderate FEs limit their applicability to bioassays whose interest concerns concentrations larger than tens of picomolar.[10]

Thus, a wide variety of nanostructured platforms have been recently explored to devise high-performance fluorescence enhancers apt to realize ultrasensitive bioassays such as nanoassemblies,[11,12] nanocages,[13,14] and nanopatterns.[15–17] Particularly, Soret colloids realized through thermo-driven self-assembly[18] represent an intriguing approach to achieve not only remarkable FEs (up to thousands-fold)[19,20] – thanks to the collective and coherent coupling between localized surface plasmons and surface plasmon polaritons –,[19,21] but also highly directional and *p*-polarized emission enhancements (> 97%) when implemented on SPCE platforms.[19,22] Even larger FEs (up to 10^6-fold)[23] were measured by using particular designs sustaining strong interplasmon coupling such as nanocavities[17,24] and nanoantennas.[25,26] However, such architectures require a nanoscale positioning of the fluorescent molecules at electromagnetic hot spots such as to make unpractical their adoption in real biosensing applications.[27]

Two-dimensional (2D) patterns of metal nanoparticles represent a smart solution to simultaneously augment both the FEs via interplasmon coupling and the hot spot density. Their optical properties strongly depend on lattice parameters and on size, shape, material and immediate environment of nanoparticles.[28] In fact, changes in the refractive index of the immediate environment entail a variation of the optical response so that nanostructured surfaces can be effectively used for bulk refractive index sensing and molecular sensing.[29–31] As it concerns the material, silver is generally preferred to gold in fluorescence-based assays because of the lower quenching entailed by silver at nanoscale distance (< 5 nm). However, the high chemical reactivity of silver makes it prone to oxidation and dissolution which results detrimental for some

applications in real matrices.[32] On the other hand, gold exhibits high biocompatibility and inertness.[33,34] Innovative strategies have been recently explored for dequenching the fluorophore emission, such as adopting photonic crystal and graphene oxide as substrates.[35,36] In this regard, photonic crystal-coupled emission (PCCE) platforms were effectively employed to reduce the quenching thereby improving the fluorescence of about 100-fold and 1500-fold with silver nanoparticles (AgNPs) and gold nanoparticles (AuNPs), respectively.[19,37]

Patterns of AuNPs are valid candidates as signal enhancer since they combine tunable plasmonic features with simple fabrication.[38–40] In a first approximation, the optical behaviour of a 2D AuNP array is closely related to the ratio D/d between the nanoparticle diameter D and the center-to-center distance d. When a nanoparticle is placed in close proximity to its nearest neighbours ($D/d \geq 2/5$),[41] the near-field interaction among the localized surface plasmons (LSPs) gives rise to a plasmonic coupled mode whose resonance is red-shifted in accordance with the hybridization model.[42,43] Such a coupled effect is negligible if $D/d < 2/5$, in which case the optical response of the array is well-described by a system of decoupled LSPs.[41]

Additionally, multi-resonant plasmonic modes can be activated by properly tailoring the pattern architecture so that these structures are suitable for multiplexed bioanalytical assays. Multiplexing-based assays are highly appealing in diagnostics since they benefit from lower detection time, sample volume and costs despite generally suffering from low sensitivity and specificity, also requiring complex microfluidic systems, sample pretreatments and purification steps.[44,45]

As it concerns the nanoparticle patterning, plenty of methods were recently developed to fabricate periodic arrays of AuNPs on large scale areas.[38,46,47] Self-assembly is an intriguing method to efficiently order a large number of nanoparticles onto macroscopic surfaces. In order to obtain arbitrary patterns, nanoparticles can be firstly self-assembled on a lithography defined

template and then transferred onto the substrate. Such a printing strategy was proven to be efficient to produce patterns of AuNPs with a single particle resolution.[48] A promising alternative is represented by colloid lithography where nanoparticles are closely packed to form a mono-layer of a periodic structure on a substrate which can be then transferred by etching or lift-off.[49,50]

When fabrication affordability and scalability as well as optical tunability are required, block copolymer micelle nanolithography (BCMN) stands out over other methods thanks to its capability to easily produce large-scale periodic arrays of AuNPs whose lattice parameters can be modified by simply choosing the appropriate diblock copolymers.[51] In recent studies, we successfully realized two plasmonic substrates consisting of hexagonally-arranged[52] (utilizing BCMN) and randomly positioned[53] AuNPs (electrostatic immobilization) apt to be implemented in PEF-based apta-immunoassay for detecting malaria biomarker *Plasmodium falciparum* lactate dehydrogenase (*Pf*LDH) in whole blood without any sample pretreatment down to picomolar and femtomolar levels, respectively.

The quest for multiplexed detection – while preserving high quality performances – spurred us to devise a double-resonant plasmonic nanostructure suitable for simultaneously detecting two different analytes in the matrix of interest. Thus, we tailored BCMN in such a way to fabricate branch patterns made of plasmon-coupled hexagonally-arranged AuNPs, which gives rise to a coupled mode whose resonance lies in the far-red region, and sprinkled plasmon-uncoupled AuNPs that exhibit a narrow LSP resonance (LSPR) at 524 nm. As a case study, we implemented the proposed plasmonic nanostructure in a PEF-based malaria apta-immunosensor for detecting *Pf*LDH in spiked whole blood. *Pf*LDH is a biomarker secreted by *Plasmodium falciparum* parasite, the most common and lethal among the malaria parasites accounting for 90% of malaria-related mortality worldwide.[54]

The PEF-based apta-immunoassay herein described combines the intrigued optical properties of a double-resonant plasmonic nanostructure with a robust antibody-functionalization strategy – the so-called photochemical immobilization technique (PIT) – capable to covalently bind antibodies (Abs) onto gold surfaces in orientated way thereby warranting that one fragment antigen-binding (Fab) site is exposed to the surrounding environment.[55,56] While Abs were preferred as capture bioreceptor layer since the simple and effective functionalization carried out via PIT, fluorescently-labelled aptamers (Apts*) were employed as top bioreceptor layer in the sandwich configuration to (i) significantly increase the specificity, (ii) enable optimal fluorophore-nanostructure distance (approximately 10 nm), and (iii) accomplish a versatile and affordable fluorescent labelling of the analytes of interest. It is worth mentioning that our approach allowed us to not be overly concerned about dequenching strategies since fluorophores were inherently positioned beyond the FRET region.

2. RESULTS AND DISCUSSION

2.1. Characterization of the substrate. *2.1.1 Morphology*. The substrate was morphologically characterized by scanning electron microscopy (SEM) (details are reported in Section S1). Figure 1a shows a SEM image at high magnification of the nanostructured pattern . Aiming to activate the plasmonic coupled modes of the AuNPs arranged along the branches, the particle growth was carried out to increase the D/d value (Figure 1b). A higher number of isolated AuNPs appears as a by-product of the growth process. Instead of representing a detriment, such isolated AuNPs trigger a localized resonance mode in addition to the coupled mode. The histogram of the nanoparticle size before the growth process includes two Gaussian distributed populations: patterned AuNPs

whose distribution is peaked at 27 nm with a standard deviation of 5 nm and isolated larger gold by-products randomly distributed onto the substrate whose size is 45 ± 7 nm (Figure 1c). The histogram after the nanoparticle growth includes three populations: isolated AuNPs whose diameter is 31 ± 6 nm, larger AuNPs of 56 ± 10 nm diameter arranged along the branches, and isolated gold by-products of 90 ± 15 nm size (Figure 1d). The centre-to-centre distance distribution of patterned AuNPs did not significantly change after the nanoparticle enlargement meaning that the growth process does not alter the patter architecture (Figures 1e and 1f). An average centre-to-centre distance of 80 nm was large enough to sustain a plasmonic coupled mode for patterned AuNPs of approximately 50-60 nm diameter.

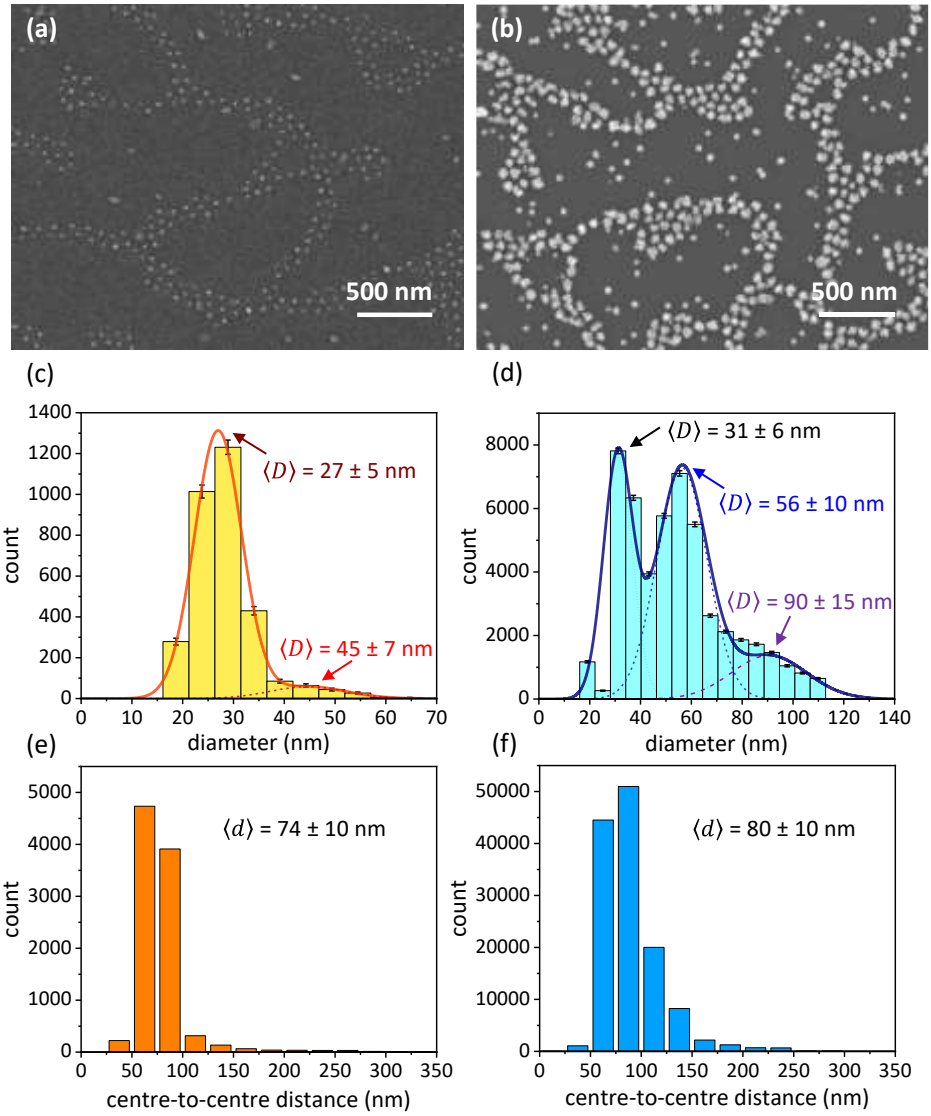

Figure 1. SEM images of the substrate (a) before and (b) after the nanoparticle growth. Histograms of the nanoparticle diameter (c) before and (d) after the nanoparticle growth. The solid orange and blue lines are the fits obtained by considering the histograms as the sum of (c) two and (d) three Gaussian distributed populations, respectively. Histograms of the centre-to-centre distance (e) before and (f) after the nanoparticle growth.

2.1.2 Optical response. The experimental extinction spectrum of the substrate contains two plasmonic resonances occurring at (i) 524 nm and (ii) 675 nm (solid black line in Figure

2). (i) Isolated AuNPs contribute to the resonance at smaller wavelength – as expected for 30 nm diameter gold nanospheres in air –[57,58] whereas (ii) patterned AuNPs give rise to a coupled mode at higher wavelength.[57] The experimental extinction spectrum is well reproduced by that one worked out by solving Maxwell's equations through finite-difference time-domain (FDTD) simulations (solid gold line in Figure 2) (technical details on FDTD simulations are reported in Section S2). For comparison, we also worked out the extinction spectra of the nanostructure without combination of AuNPs with different size (see Section S3).

Once the substrate was optically characterized, the fluorophore should be generally chosen so that its excitation/emission peaks overlap with the plasmon extinction.[1,8] Given the large variety of organic fluorophores apt to this aim, the spectral overlap may be virtually accomplished at any wavelengths in the visible range. In this regard, we selected 5-carboxyfluorescein (5-FAM) and cyanine 5 (Cy5) dyes whose excitation/emission spectra are reported in Figure 2. While the narrow resonance at 524 nm restricts the spectral overlap to the only radiative coupling with 5-FAM dye (emission peak at 520 nm, dashed green line), the broad resonance band at higher wavelengths leads to a dual-mechanism coupling with Cy5 dye (excitation/emission 650 nm/665 nm, dashed orange and red lines).

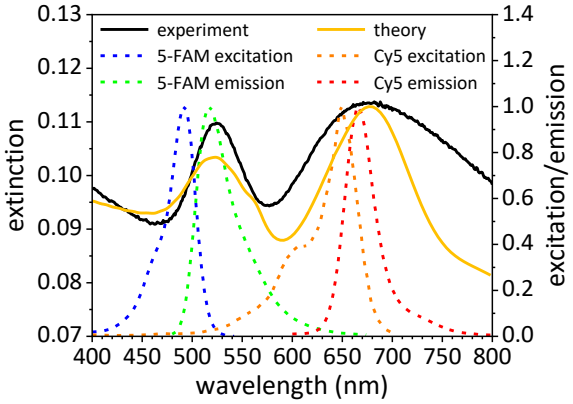

Figure 2. Experimental (solid black line) and theoretical (solid gold line) extinction spectrum of the substrate. Plasmon-fluorophore spectral overlap with 5-FAM (emission coupling, dashed green line) and Cy5 (dual-mechanism coupling, dashed orange and red lines) dyes.

It is worth mentioning that the choice of 5-FAM dye was not optimal since its excitation peak lied off-resonance (490 nm). In such a way, we did not fully exploit the amplification potential of the plasmonic resonance at 524 nm. Indeed, a fluorophore whose excitation peak was in the green band may experience a higher FE as compared to 5-FAM dye.

2.2. Apta-immunoassay sensing performance. *2.2.1. Gold surface biofunctionalization by PIT.* The substrates were functionalized with pan malaria Abs (anti-*P*LDH) by using PIT. Firstly, the concentration of anti-*P*LDH was varied over large intervals so to optimize the surface covering (Figure S4a). The shift of the plasmon resonance wavelength $\Delta\lambda$ showed no significant variations for concentrations larger than 50 μg/mL, that is a threshold above which no more free gold surface is available for the Ab anchoring. Thus, an anti-*P*LDH concentration of 50 μg/mL was used throughout all the experiments yielding a plasmon red-shift of approximately 4-5 nm due to the dielectric protein layer surrounding the AuNPs (Figure S4b). The close-packed covering is also evident by the lack of any significant

optical change in the extinction spectrum after the blocking step (dashed red line in Figure S4b). By considering a steric hindrance of a single immobilized Ab equal to ~150 nm^2,[59] the Ab density (number of Abs per AuNP) was estimated as ~75 (~20) for nanospheres of 60 nm (30 nm) diameter.

2.2.2. Detection scheme. This work was conceived as a case study for evaluating the performance of the proposed substrate as a fluorescence enhancer in PEF-based biosensor in multiplexed measurements for simultaneously detecting two different analytes. The multiplexed detection was obtained by adopting the sandwich configuration Ab-analyte-Apt* shown in Figure 3a. The capture bioreceptor layer was realized by well-oriented Abs with one Fab exposed to the surrounding environment thanks to the PIT functionalization thereby significantly increasing the effectiveness of the analyte binding. Two kinds of labelled aptamers (with green and red probes) were used as recognition bioreceptor layer to explore the double-resonance of the branch pattern.

Figure 3b shows some examples of fluorescence images recorded at different *Pf*LDH concentrations, in which the number of bright spots is strikingly higher as compared to the control (i.e., uninfected human whole blood) down to 1 pM (35 pg/mL) for both the fluorophores (full details about acquisition and processing of fluorescence pictures are reported in Section S5). Note that the fluorescence of each bright spot is likely to arise from one single fluorophore as explained in detail in Section S6.

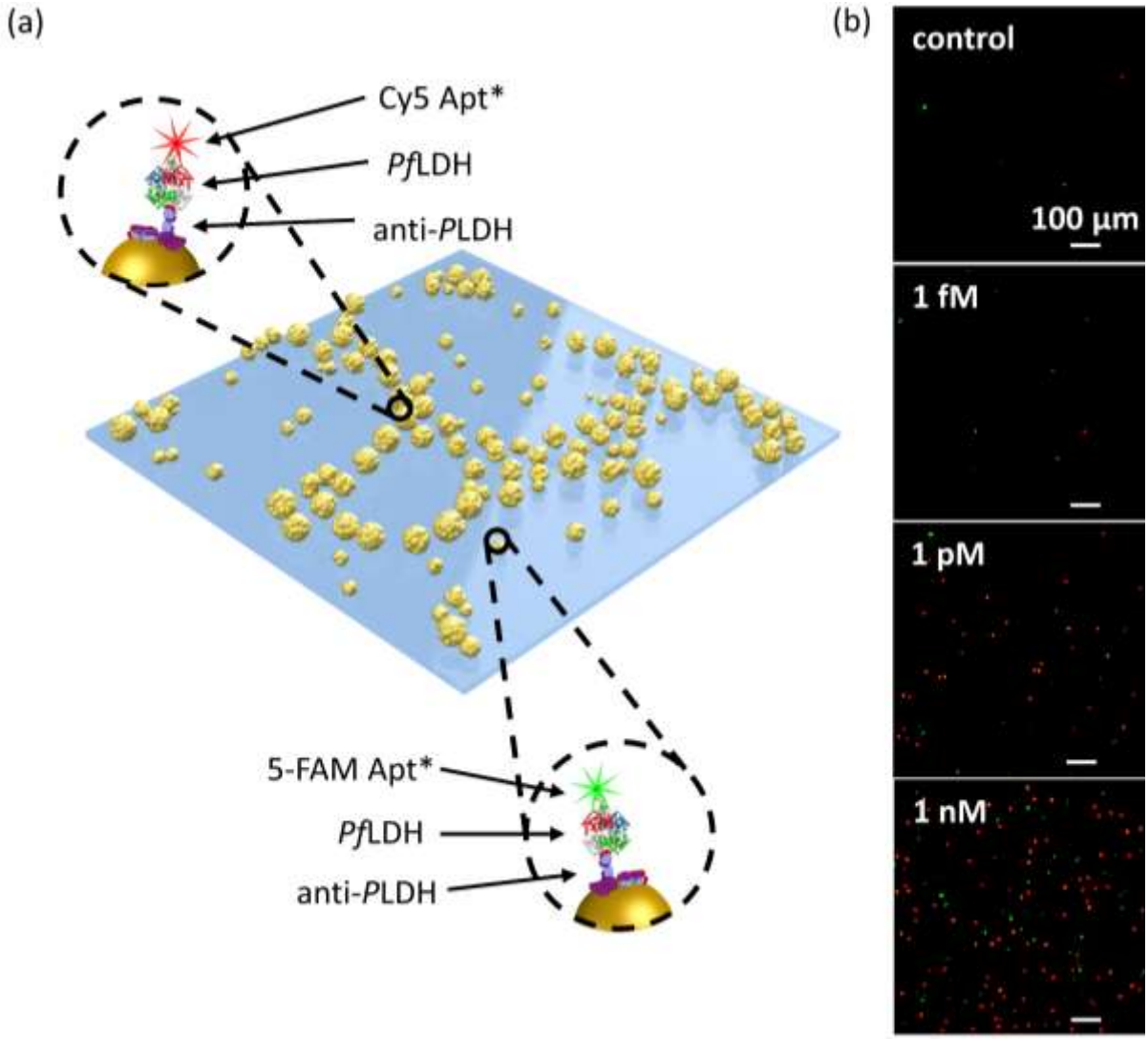

Figure 3. (a) Sketch of the pattern architecture consisting of branch hexagonally-arranged and sprinkled AuNPs. The insets show the Ab-*Pf*LDH-Apt* sandwich schemes in the case of 5-FAM and Cy5 labels. (b) Example of fluorescence images recorded at different *Pf*LDH concentration spiked in human whole blood.

2.2.3. Calibration curves. The fluorescence intensity F as a function of the analyte concentration is shown in Figure 4a (details about fluorescence analysis are reported in Section S5). The data are well fitted by the four-parameter Hill equation[60]

$$F([Pf\text{LDH}]) = F_1 + \frac{F_2 - F_1}{1 + \left(\frac{K}{[Pf\text{LDH}]}\right)^n} \quad (1)$$

where F_1 and F_2 are the minimum and maximum value of the fluorescence intensity, respectively, K is the concentration at which the fluorescence reaches its half-maximum value, and n is the so-called Hill's coefficient.[61] Table 1 reports the best-fit parameter values, the linear range (LR), and the limit of detection (LOD) – estimated as 3σ above the control value – for both the fluorescent dyes used in this work.

Table 1. Best-fit parameter values, LR, and LOD obtained by fitting the experimental data of Figure 4a with Equation (1).

Parameter	5-FAM	Cy5
F_1	7 ± 1 arb. units	6 ± 2 arb. units
F_2	66 ± 3 arb. units	154 ± 4 arb. units
K	(0.36 ± 0.15) × 10^3 pM	6 ± 1.7 pM
n	0.36 ± 0.05	0.44 ± 0.06
χ^2	1.2	1.8
LR	10 pM-1 μM	100 fM-1 nM
LOD	50 pM (1.6 ng/mL)	260 fM (8.6 pg/mL)

For comparison, we listed in Table 2 some recently reported platform-based biosensors for multiplexed measurements. It is worth noticing that in many applications the multiplexing was realized by performing parallel measurements on one platform containing different chips, each of them devoted to one analyte of interest. However, although such an approach constitutes a smart strategy to achieve multiplexed analysis without sophisticate

multi-response chips, it may require complex microfluidic systems or an increase of specimen amount and costs.[44,45] On the contrary, chips exhibiting multi-responsivity only need one specimen to carry out multiplexed analysis thereby reducing materials and costs.[62,63]

Table 2. Overview on recently reported platform-based biosensors for multiplexed analysis.

Platform	Method	Matrix	Analytes	LR (pM)	LOD (pM)
AuNPs-modified screen-printed carbon electrode	EIS	Protease solution	*Listeria. monocytogenes*	$10\text{-}10^7$ CFU mL^{-1}	9 CFU mL^{-1}
			Staphylococcus aureus		3 CFU mL^{-1}
Nanostructured conductive hydrogel electrodes on PET film	Amperometry	Human serum	Triglycerides	$0.1\text{-}6 \times 10^9$	7×10^7
			Lactate	$0.08\text{-}5 \times 10^9$	6×10^7
			Glucose	$1\text{-}25 \times 10^9$	2×10^8
Glass	Interferometry	Human serum	Anti-thyroglobulin IgG	1.7-860 IU mL^{-1}	6 IU mL^{-1}
			Anti-thyroid peroxidase IgG		1.7 IU mL^{-1}
Au triangular nanoprisms on MPTMS functionalized glass coverslip	LSPR	Human plasma	microRNA-10b	$10^{-4}\text{-}10^4$	5.9×10^{-5}
			microRNA-96		8.9×10^{-5}
			microRNA-145		2.12×10^{-4}
			microRNA-143		1.86×10^{-4}
			microRNA-490-5p		1.83×10^{-4}
AgNP film on silicon wafer	Raman spectroscopy	PBS	α-fetoprotein	5.9-4300	0.1 [(b)]
			Glypican-3		
Au core–SERS label–Ag shell–Au shell on silicon wafer	Raman spectroscopy	PBS	Microcystin-LR	$10\text{-}10^4$	1.5
			Microcystin-RR		1.3
Au-coated grating	Fluorescence	PBS (1 mg/mL BSA)	Anti-mouse IgG-AF790	0.01-5	6×10^{-3}
Branch pattern of AuNPs on glass coverslip	Fluorescence	Human whole blood	*Pf*LDH-5-FAM	$10\text{-}10^6$	50
			*Pf*LDH-Cy5	$0.1\text{-}10^3$	0.26

Remarks	Ref.
Multiplexed measurements were performed on a microarray of four electrodes functionalizing each of them accordingly to the analyte of interest.	68
Multiplexed measurements were performed on a pre-screen-printed electrode unit containing three screen-printed carbon paste working electrodes. Each electrode was functionalized against the analyte of interest.	67
Multiplexed measurements were performed on a multi-spot sensor chip functionalizing each spot properly.	66
Multiplexed measurements were carried out in a 96-well plate. Each well was used for detecting one analyte.	44
LR and LOD were estimated in 100× diluted samples. Thus, the results should be worsened by two orders of magnitude when referred to real samples.	65
Multiplexed measurements were performed on one chip functionalized with two different probes consisting of aptamer-driven core–satellite assemblies.	63
Multiplexed measurements may be carried out on one chip by using microfluidic channels.	64
The effectiveness of multiplexed analysis was demonstrated by evaluating the double-response of the chip with two fluorescent tags labelling one kind of analyte.	This work

S: sensitivity, EIS: electrochemical impedance spectroscopy, PET: polyethylene terephthalate, MPTMS: (3-Mercaptopropyl)-trimethoxysilane, PBS: phosphate-buffered saline, BSA: bovine serum albumin, AF790: Alexa Fluor 790. Markers: (*a*) data not given in the reference, the value was estimated by calibration curve, (*b*) LOD not given in the reference, the value reported in table corresponds to the lowest measured analyte concentration.

2.2.4. Specificity. The specificity of the proposed apta-immunosensor was tested against the *Plasmodium vivax* lactate dehydrogenase (*Pv*LDH), which shares 90% residue identity with the *Pf*LDH.[69] The *Pv*LDH was spiked into the uninfected human whole blood (1:100 diluted in 1 mL of 25 mM Tris buffer) to obtain the highest analyte concentration explored in the calibration curve (1 μM referred to undiluted whole blood). Figure 4b shows the fluorescence intensity measured in human whole blood with no analyte (control), competitive analyte (*Pv*LDH), and analyte of interest (*Pf*LDH). Although the bottom bioreceptor layer – consisting of pan malaria anti-*P*LDH – can capture any *Plasmodium* malaria marker, no significant cross-reaction was detected in the case of *Pv*LDH thanks to the extremely high specificity of the aptamers used as top bioreceptor layer.[70]

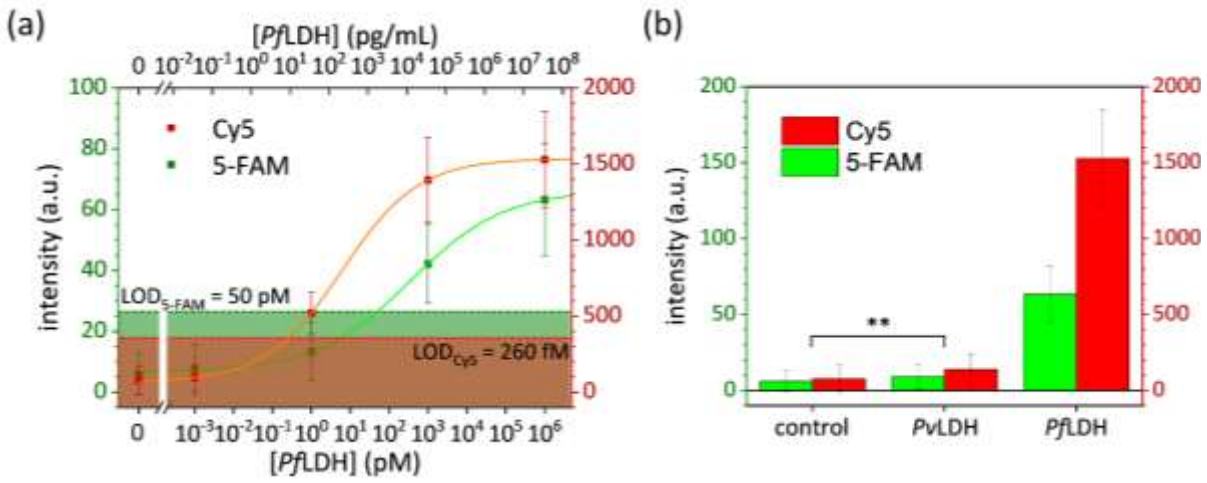

Figure 4. (a) Calibration curve (fluorescence intensity vs *Pf*LDH concentration spiked in human whole blood) of the apta-immunoassays for *Pf*LDH concentration in the range 1 fM to 1 μM (0.03 pg/mL to 0.03 mg/mL). The data are best fitted by the four-parameter Hill Equation (1) (solid green and orange lines). The shaded regions represent the 3σ noise level measured in uncontaminated whole blood. (b) Specificity of the apta-immunoassay against the *Pv*LDH (**p-value < 0.001). The data are presented as mean value ± standard deviation and are representative of ten technical repeats.

2.3. Fluorescence enhancement. *2.3.1. Electromagnetic simulations*. We investigated the electromagnetic response of the substrate when interacting with a plane wave radiation $\mathbf{E_0}$. The ratio between the intensity of the electric field induced by the nanostructure, $\mathbf{E}$, and the intensity of the incident radiation is defined as the gain factor G[71]

$$G(\omega, \mathbf{r}) = \frac{|\mathbf{E}(\omega, \mathbf{r})|^2}{|\mathbf{E_0}(\omega, \mathbf{r})|^2} \quad (2)$$

where ω is the frequency of the impinging perturbation and $\mathbf{r}$ is the position vector.

We modelled the nanostructure accordingly to the architecture morphology provided by SEM images. In addition, we implemented a surface roughness onto each nanoparticle to

approach the observed nanoparticle shape (see Section S2.B for details). Since the size of the fluorophores we used is ~1 nm^3,[72] we discretized the substrate over a mesh with 1 nm spatial resolution so that a dye can fit in a unit cell. Figures 5a-c show the intensity distributions of the electric field at the emission peak of 5-FAM (520 nm) and at the excitation/emission peaks of Cy5 (650/665 nm), whereas those worked out off-resonance (490 nm and 575 nm) are depicted in Figure S7.

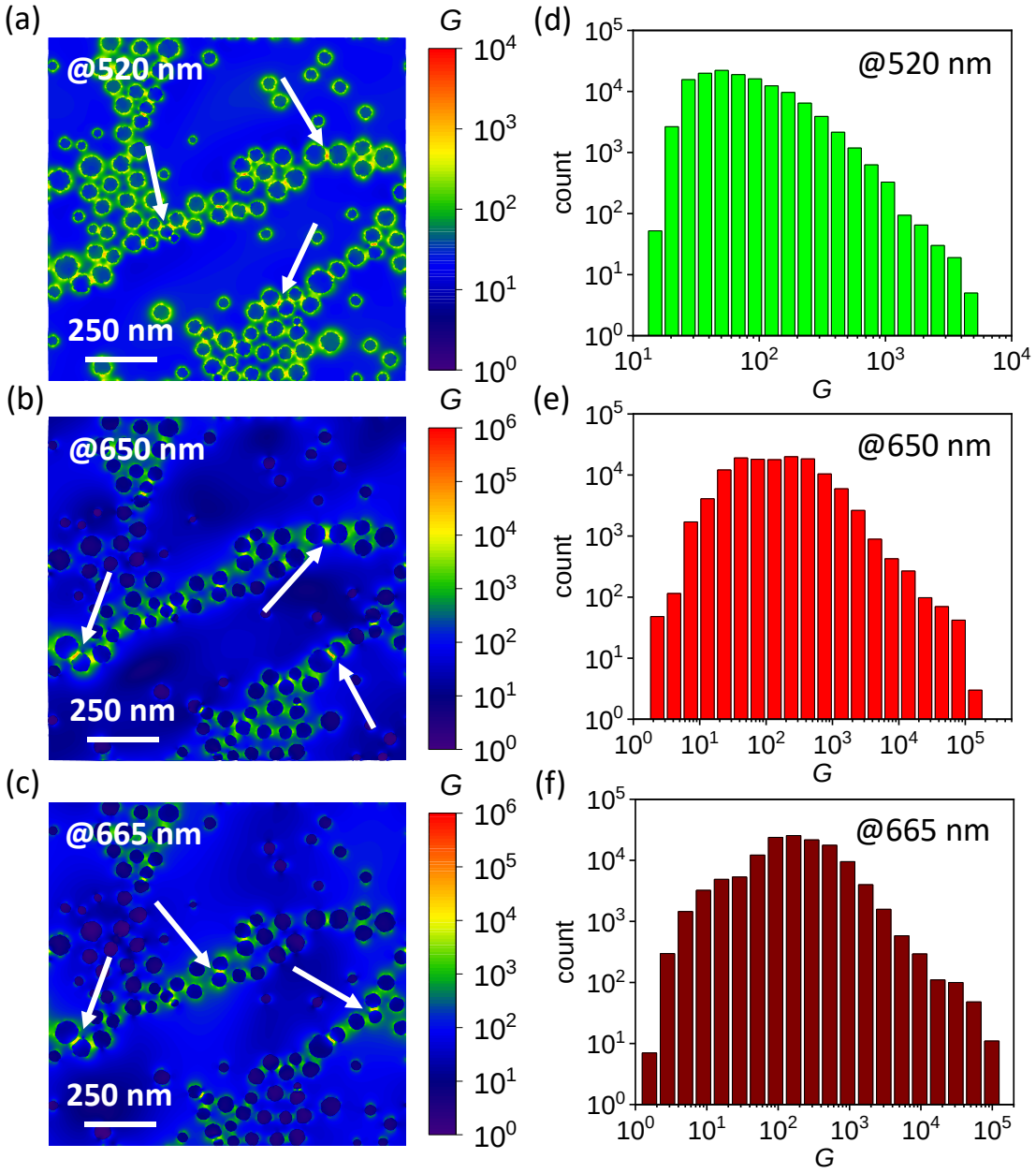

Figure 5. Simulated electric field intensity of the substrate worked out at wavelength (a) 520 nm, (b) 650 nm, and (c) 665 nm. The white arrows point to some plasmonic hot spots of the nanostructure. Histograms of the G value distribution evaluated in annulus-shaped regions around nanoparticles (5 nm thickness, 5 nm offset from particle surface) at wavelength (d) 520 nm, (e) 650 nm, and (f) 665 nm.

Regions surrounding nanoparticles exhibit higher G values as compared to the free space as a result of the strong confinement of the electric field: These regions are generally called hot spots.[71]

At 520 nm wavelength the main contribution to the electric field arose from the dipolar modes of nanoparticles. In this case, the electric field was mainly enhanced at the nanoparticle edges (along the polarization direction) or confined at the nanoparticle dimer junctions (Figure 5a). However, such a plasmonic mode (i.e., not coupled mode) yielded a relatively low amplification (G values do not exceed few thousand). On the contrary, much higher G values (up to hundreds of thousands) were observed at 650 nm and 665 nm wavelengths as a result of the strong interplasmon coupling among nearby AuNPs (Figures 5b and 5c). The physics underlying the coupled modes can be captured by exploring the optical properties of nanoparticle dimers via the so-called plasmon hybridization method,[42,73] according to which the localized surface plasmons hybridize to form bonding and antibonding plasmonic modes.[43]

Since we aimed at using this platform for sensing applications where fluorophores are placed at a distance of 5-10 nm from the nanoparticle surface, we focused our analysis on these annulus-shaped regions around each nanoparticle (details are reported in Section S8). Figures 5d-e show the G value distributions in these regions at wavelength 520 nm, 650 nm and 665 nm, respectively. The histograms reveal that only a tiny fraction of fluorophores would experience a relatively high G value meaning that most of them were positioned in places whose local amplification may not be strong enough to yield a measurable fluorescence.

Additionally, we worked out the electromagnetic response of the substrate with perfectly spherical nanoparticles (see Section S2.A for details). In this case, much lower G values were attained revealing that the surface roughness was a crucial feature to augment the local field (Figure S9).[74] For comparison, we also investigated the electromagnetic response of different nanoparticle shape and material in isolated and hexagonally-arranged configurations.[75] For futuristic scope, it is worth mentioning that up to 100-fold amplification could be potentially achieved with sharp silver nanoparticles as compared to smooth gold nanoparticles (see Section S10).

2.3.2. Comparison between theoretical and measured fluorescence enhancement. The FE factor is defined as[71]

$$FE^{\mathrm{th}}(\omega,\omega') = G(\omega)\frac{QY(\omega')}{QY^{0}(\omega')} \tag{3}$$

where QY is the fluorophore quantum yield in PEF conditions, QY^0 is the fluorophore quantum yield in free-space, ω and ω' are the excitation and emission frequency, respectively. We aimed at comparing the FE^{th} values at excitation/emission wavelengths of the fluorophores with those experimentally measured (later described). Since QY^0 is an inherent parameter of the fluorophore, the ratio QY/QY^0 is bounded above due to the constraint $QY \leq 1$. Considering QY^0_{5FAM} = 0.83 at 520 nm wavelength for 5-FAM dye[76] and QY^0_{Cy5} = 0.27 at 665 nm wavelength for Cy5 dye[77], the ratio QY/QY^0 cannot exceed 1.2 for 5-FAM dye and 3.7 for Cy5. For simplicity, we firstly investigated the case $QY = QY_0$. Thus, the G value distributions shown in Figures S7c and 5e can be immediately converted into $\overline{FE}^{\mathrm{th}}$ distributions at 490/520 nm and 650/665 nm excitation/emission, respectively.

As it concerns the measured FE factor, it can be estimated as[78]

$$FE^{\mathrm{obs}} = \frac{I_{\mathrm{PEF}}}{\langle I_0 \rangle} \tag{4}$$

where I_{PEF} is the fluorescence intensity provided by fluorophores in presence of the nanostructure and $\langle I_0 \rangle$ is the mean fluorescence signal of fluorophores under non-PEF conditions (details are reported in Section S11). Figures 6a and 6b show the FE^{obs} distributions for 5-FAM and Cy5 dyes, respectively (patterned histograms). Thus, we can compare such distributions with $\overline{FE}^{\mathrm{th}}$ distributions (shaded histograms).

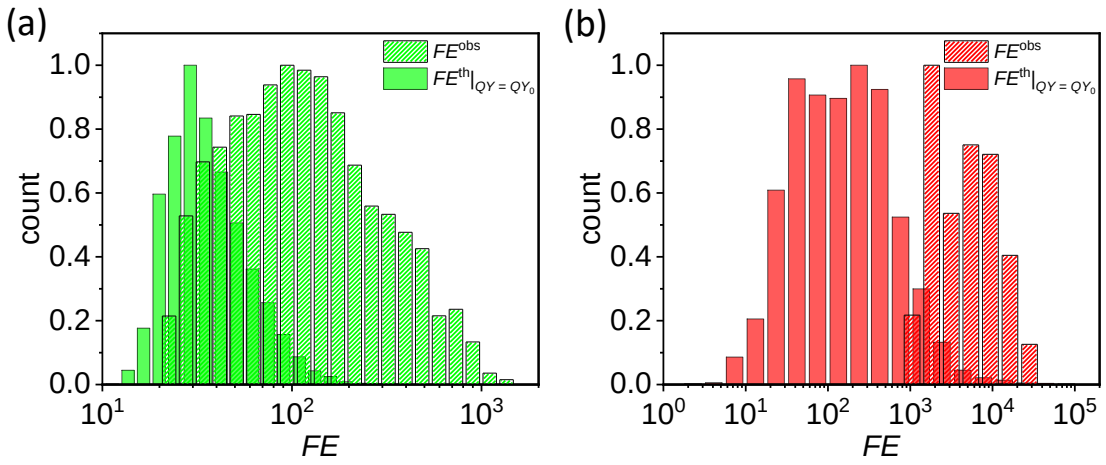

Figure 6. Experimental (patterned histograms) and theoretical (shaded histograms) FE distributions for (a) 5-FAM and (b) Cy5 dyes. Theoretical distributions are worked out at (a) 490/520 nm and (b) 650/665 nm excitation/emission wavelengths in the case $QY = QY_0$.

It is worth mentioning that even if we consider the highest emission enhancement (i.e., $QY = 1$), a slight discrepancy would emerge in both the fluorophore channels (more prominent in the 5-FAM channel) probably ascribable to an ineffective nanoparticle roughness in the simulation modelling. Note that such a discrepancy would rise if perfectly spherical nanoparticles were considered rather than rough nanoparticles thus corroborating the crucial role played but the nanoparticle roughness in enhancing the fluorescence.

An estimation of the average FE factor, $\langle FE^{\mathrm{obs}} \rangle$, can be retrieved by[78]

$$\langle FE^{\mathrm{obs}} \rangle = \frac{\sum_{k=1}^{N_{\mathrm{PEF}}} (I_{\mathrm{PEF}})_k}{\langle I_0 \rangle \, N_{\mathrm{PEF}}} \tag{5}$$

where N_{PEF} is the number of bright spots. Equation (4) yields $\langle FE_{\mathrm{5FAM}}^{\mathrm{obs}} \rangle$ = 160 for 5-FAM dye and $\langle FE_{\mathrm{Cy5}}^{\mathrm{obs}} \rangle$ = 5200 for Cy5 dye.

3. CONCLUSIONS

In this paper, we presented a novel double-resonant plasmonic substrate for potential multiplexed and high-throughput analysis in PEF-based biosensing. The substrate consists of an assembly of hexagonally-arranged and sprinkled AuNPs, which gives rise to a double resonance at 524 nm and 675 nm wavelengths. The former was coupled with the emission peak of 5-FAM dye and the latter with both the excitation and emission peaks of Cy5 dye. Numerical simulations demonstrated that the pattern architecture endowed the substrate with a large number of intense electromagnetic hot spots in which fluorophores can be housed.

The substrate was implemented in a malaria apta-immunoassay for detecting *Pf*LDH in human whole blood. We adopted Abs as capture bioreceptor layer and Apts* as top fluorescently-labelled layer. Substrate functionalization was realized through PIT, which warranted that Abs covalently tethered to nanoparticle surfaces in well-oriented configuration. In addition, the adoption of Apts* rather than fluorescently-labelled Abs drastically reduced the cost per assay while improving the specificity. The *Pf*LDH was simultaneously detected by both the fluorophores as proof of concept for multiplexed analysis. Additionally, the simultaneous detection of two fluorescent probes can provide high signal redundancy and an extension of the detection range.

We achieved competitive LODs of 260 fM with Cy5 dye and 50 pM with 5-FAM dye. No complex sample pretreatments are required making such a device suitable for point of care tests.

The measured average FE values of 160 (with 5-FAM dye) and 5200 (with Cy5 dye) are consistent with those simulated by considering branch patterns of rough AuNPs. It is worth mentioning that the LOD may be improved up to 100-fold in a transparent matrix such as human serum or plasma since 1:100 dilution required for whole blood would be not necessary.

Finally, the BCMN fabrication technique is extremely versatile allowing one to easily tune the plasmonic response in the visible range. As futuristic scope, multi-resonant devices may be also conceived by properly tailoring the pattern architecture or combining different metal nanoparticles in such a way to active additional plasmonic modes. Moreover, sharp nanoparticles may further augment the electromagnetic field by at least one order of magnitude as compared to smooth nanoparticles as simulations revealed. The potential biosensing applications of the proposed approach are far-reaching, for not only multi-analyte detection but also biomarker panel identification with double signal redundancy.

4. EXPERIMENTAL SECTION

4.1. Chemicals and materials. Gold(III) chloride trihydrate ($HAuCl_4 \cdot 3H_20$), silver nitrate ($AgNO_3$), ascorbic acid and toluene (99.8%) were purchased from Sigma-Aldrich; ethanol (≥ 99.5%), 2-propanol (≥ 99.5%) and acetone (≥ 99.0%) were purchased from Merck Millipore; hexadecyltrimethylammonium bromide (CTAB) (≥ 99.0%) was purchased from Fluka; bovine serum albumin (BSA) (fraction V IgG free, fatty acid poor) was purchased from Gibco. Diblock copolymers (P3807-S2VP) were purchased from Polymer Source Inc. (Dorval, Canada) and were made by polystyrene(x)-b-2-poly-vinylpyridine(y) (PS(x)-b-P2VP(y)), in which x = 325000 g/mol and y = 92000 g/mol are the molecular weight of polystyrene (PS) and poly(2-vinylpyridine) (P2VP), respectively. Ultrapure deionized

water used for all aqueous solutions was dispensed by Milli-Q® system (18.2 MΩ cm resistivity). 10 mM phosphate-buffered saline (PBS) (NaCl 10 mM, NaH_2PO_4 10 mM, Na_2HPO_4 10 mM, $MgCl_2$ 1 mM, pH 7.1) and 25 mM Tris-HCl buffer (NaCl 100 mM, imidazole 20 mM, Tris 25 mM, HCl 25 mM, pH 7.5) were prepared by dissolving the reagents (purchased from Sigma-Aldrich) in ultrapure water. Pan malaria antibody (monoclonal anti-*P*LDH antibody clone 19g7) was produced by Vista Laboratory Services (Langley, USA). The recombinant *Pf*LDH and *Pv*LDH were obtained from bacterial expression as previously described.[70] The malaria 2008s aptamer labelled with 5-FAM (analogously, Cy5) tag (5'-5-FAM(Cy5)-CTG GGC GGT AGA ACC ATA GTG ACC CAG CCG TCT AC-3') was synthesized by Friz Biochem GmbH (Neuried, Germany). Millex® syringe filters (pore size 0.20 μm) with hydrophilic polytetrafluoroethylene membrane were purchased from Merck Millipore; Superslip™ cover slips (borosilicate glass, thickness 0.13-0.17 mm) were purchased from Thermo Fisher Scientific.

4.2. Substrate fabrication and characterization. *4.2.1. Fabrication of branch patterns of AuNPs.* BCMN was adopted to fabricate branch patterns of hexagonally-arranged AuNPs over large area.[51] The procedure included four steps schematically shown in Figure 7.

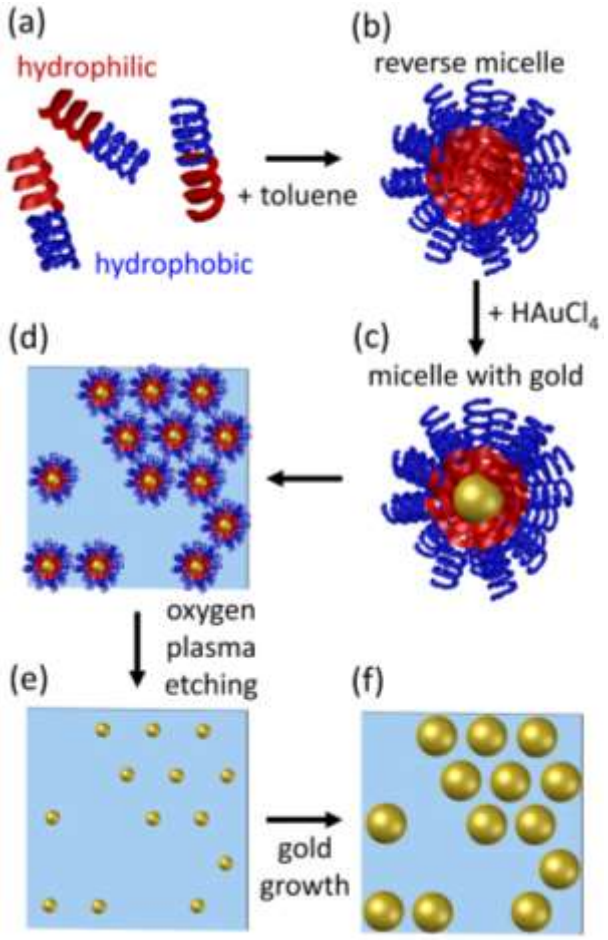

Figure 6. Fabrication scheme of branch pattern of AuNPs by BCMN. (a) Dispersion of amphiphilic diblock copolymers in nonpolar solvent. (b) Formation of reverse micelles consisting of hydrophilic core and hydrophobic shell. (c) Formation of gold seeds inside the micelle core. (d) Laying of PS-AuNPs on the substrate. (e) Sticking of the AuNPs onto the substrate after the copolymer etching. (f) Enlargement of the nanoparticle size.

An amount of 24.3 mg of diblock copolymer P3807-S2VP (Figure 7a) was dispersed into 15 mL of toluene under vigorous stirring for 72 h so to obtain homogeneous monodisperse solution of reverse micelles (Figure 7b). An amount of 13.1 mg of $HAuCl_4 \cdot 3H_20$ was loaded into the solution under vigorous stirring for 72 h allowing the formation of gold seeds covered by polystyrene shells (PS-AuNPs) (Figure 7c). Then, the yellowish solution

was filtered to remove possible copolymer aggregates. Diblock copolymers and gold(III) chloride trihydrate were handled in a glovebox under inert gas (argon) and controlled conditions (O_2 < 1 ppm, H_2O < 0.1 ppm).

Before PS-AuNP deposition onto the substrate, glass coverslips (10 × 8 mm^2) were cleaned by sonication for 5 min in acetone, 2-propanol, and ethanol sequentially, and dipped in nonpolar solvent to enable the sticking of hydrophobic polystyrene shells. Then, the substrate was finely dipped into the PS-AuNP solution by dip-coater with a dipping speed of 0.8 mm/s. Such a speed is low enough to warrant PS-AuNP laying onto the substrate while preventing the maximum close-packing (Figure 7d). Finally, the copolymers were etched by oxygen plasma treatment (0.8 mbar, 200 W, 30 min) leaving the AuNPs immobilized onto the substrate (Figure 7e).

Afterwards, the substrate was incubated with 2 mL of gold growth solution (CTAB 190 mM, $HAuCl_4 \cdot 3H_20$ 42 mM, $AgNO_3$ 8 mM, ascorbic acid 100 mM) for 2 h enabling the increase of AuNP size while holding centre-to-centre distances (Figure 7f).[38]

4.2.2. Analysis of scanning electron micrograph. Full details are reported in Section S1.

4.2.3. Numerical simulations. Technical details on FDTD simulations are reported in Section S2.

4.3. Fluorescence apta-immunoassay. *4.3.1. Surface biofunctionalization and blocking.* Gold surface functionalization with pan malaria anti-*P*LDH was realized through the well-established PIT.[55,56] Such a technique consists of UV irradiation of Abs that produces the selective photoreduction of the disulfide bridge in specific cysteine-cysteine/tryptophan (Cys-Cys/Trp) triads,[79] which are a typical structural feature of the immunoglobulin G (IgG).[80] The UV excitation of the Trp residue leads to the generation of solvated electrons

that are captured by the nearby disulphide bridge resulting in its destabilization and subsequent breakage of the Cys-Cys bond. The breakage of such Cys-Cys bonds in both Ab Fab fragments produces four free thiol groups (Figure S12a), two of which are able to interact with the proximal gold surface giving rise to a covalent Ab tether. Functionalization by PIT assures both close-packing and control over the orientation of the immobilized Abs, with one of their binding sites exposed to the surrounding environment (Figure S12b).

The UV source (Trylight, Promete S.r.l.) consisted of two U-shaped low-pressure mercury lamps (6 W at 254 nm) in which a standard 10 mm quartz cuvette could be easily housed (Figure S12c). By considering the wrapping geometry of the lamps and the proximity of the cuvette, the irradiation intensity used for the thiol group production was approximately 0.3 W/cm^2. Such an intensity is low enough to avoid any significant photolysis of the disulfide bridge that poorly absorbs at 254 nm.[81]

A volume of 1 mL aqueous solution of anti-*P*LDH (50 μg/mL) was irradiated for 30 s and then flowed onto the substrate. The latter was integrated in a microfluidic circuit consisting of a cell containing the substrate, a 2 mL syringe, and Tygon tubes with a diameter of 1 mm (for both the input and output channel) designed for biological samples (Figure S13). The volume of the solution in contact with the substrate was ∼30 μL, whereas the total volume flowing into the circuit was approximately 200 μL. The syringe was used to repeatedly draw 250 μL from the fresh solution containing the irradiated Abs (4 draws separated by a time interval of 3 min). Then, the substrates were rinsed by ultrapure water to remove the unbound Abs.

As it concerns the blocking of the free gold surface, 1 mL of BSA aqueous solution (50 μg/mL) was flowed to prevent nonspecific adsorption (4 draws of 250 μL separated by a

time interval of 1 min). Afterwards, the samples were copiously rinsed by ultrapure water and stored in PBS solution (10 mM) at room temperature until the use (see Section S14 for details about PBS preparation).

4.3.2. Ab-analyte-Apt stacking.* Blood specimens were taken from the healthy donators via a monovette tube containing ethylenediaminetetraacetic acid to prevent coagulation. Whole blood was diluted 1:100 in 25 mM Tris buffer to reduce the turbidity of the sample (see Section S14 for details about Tris buffer preparation). The desired amount of *Pf*LDH was spiked into 1 mL of diluted whole blood to obtain analyte concentrations lying in the range 1 fM – 1 μM (referred to undiluted whole blood). Control experiments were performed in uninfected human whole blood (1:100 diluted in 25 mM Tris buffer). Anti-*P*LDH-functionalized substrates were incubated with 1 mL of spiked-blood by gently shaking the sample for 2 h to improve the *Pf*LDH capture efficiency by immobilized Abs. Then, the substrates were copiously rinsed by Tris buffer (25 mM) and ultrapure water to remove unbound proteins and blood residues.

5-FAM- and Cy5-labelled malaria Apts* were added in the ratio 1:1 into 1 mL of PBS (10 mM) to obtain a final Apt* concentration of 0.1 μM. Thus, the substrates were transferred into the solution by gently shaking the bowl for 2 h in dark condition thereby realizing the Ab-*Pf*LDH-Apt* sandwich scheme shown in Figure 3a. Then, the substrates were abundantly rinsed by PBS (10 mM) and ultrapure water to remove unbound Apts*.

4.3.3. Fluorescence picture processing and analysis. Full details are reported in Section S5.

ASSOCIATED CONTENT

Supporting Information. Analysis of scanning electron micrographs (Section S1). Coding of numerical simulations (Section S2). Optical response of homogeneously sized gold nanoparticles (Section S3). Substrate biofunctionalization (Section S4). Fluorescence picture acquisition, processing and analysis (Section S5). Analysis of the bright spots (Section S6). Off-resonance simulations (Section S7). Analysis of the electric field (Section S8). Electromagnetic response of the substrate with perfectly spherical nanoparticles (Section S9). Electromagnetic response of non-spherical nanoparticles (Section S10). Fluorescence intensity in non-PEF conditions (Section S11). Photochemical immobilization technique (Section S12). Microfluidic system (Section S13). Preparation of buffer solutions (Section S14).

AUTHOR INFORMATION

Corresponding Authors

Raffaele Velotta – Email: rvelotta@unina.it.

Dirk Mayer – Email: dirk.mayer@fz-juelich.de.

Author Contributions

A.M., B.DV., R.V., and D.M. conceived the project. A.M. carried out the experiments and collected the data under D.M. and A.O. supervision and administration. A.M. and E.S. worked out the numerical simulations. A.M., E.S., B.DV. performed the data interpretation. J.A.T. and D.M. provided support on the use of aptamers. A.M. and E.S. wrote the manuscript. R.V., D.M. and J.A.T. revised the manuscript.

Note

The authors declare no competing financial interest.

Funding Sources

ACKNOWLEDGMENT

We would like to thank Ruoyan Wei for her help on substrate fabrication through block copolymer micelle nanolithography and Gabriela Figueroa Miranda for her advices on aptamer handling.

REFERENCES

(1) Li, J. F.; Li, C. Y.; Aroca, R. F. Plasmon-Enhanced Fluorescence Spectroscopy. *Chem. Soc. Rev.* **2017**, *46* (13), 3962–3979. https://doi.org/10.1039/c7cs00169j.

(2) Ranjan, R.; Esimbekova, E. N.; Kirillova, M. A.; Kratasyuk, V. A. Metal-Enhanced Luminescence: Current Trend and Future Perspectives- A Review. *Anal. Chim. Acta* **2017**, *971*, 1–13. https://doi.org/10.1016/j.aca.2017.03.051.

(3) Cardinal, M. F.; Vander Ende, E.; Hackler, R. A.; McAnally, M. O.; Stair, P. C.; Schatz, G. C.; Van Duyne, R. P. Expanding Applications of SERS through Versatile Nanomaterials Engineering. *Chem. Soc. Rev.* **2017**, *46* (13), 3886–3903. https://doi.org/10.1039/c7cs00207f.

(4) Yang, X.; Sun, Z.; Low, T.; Hu, H.; Guo, X.; García de Abajo, F. J.; Avouris, P.; Dai, Q. Nanomaterial-Based Plasmon-Enhanced Infrared Spectroscopy. *Adv. Mater.* **2018**, *30* (20), 1704896. https://doi.org/10.1002/adma.201704896.

(5) Badshah, M. A.; Koh, N. Y.; Zia, A. W.; Abbas, N.; Zahra, Z.; Saleem, M. W. Recent Developments in Plasmonic Nanostructures for Metal Enhanced Fluorescence-Based Biosensing. *Nanomaterials* **2020**, *10* (9), 1–22. https://doi.org/10.3390/nano10091749.

(6) Lucas, E.; Knoblauch, R.; Combs-Bosse, M.; Broedel, S. E.; Geddes, C. D. Low-

Concentration Trypsin Detection from a Metal-Enhanced Fluorescence (MEF) Platform: Towards the Development of Ultra-Sensitive and Rapid Detection of Proteolytic Enzymes. *Spectrochim. Acta Part A Mol. Biomol. Spectrosc.* **2020**, *228*, 117739. https://doi.org/10.1016/j.saa.2019.117739.

(7) Chen, Y.; Munechika, K.; Ginger, D. S. Dependence of Fluorescence Intensity on the Spectral Overlap between Fluorophores and Plasmon Resonant Single Silver Nanoparticles. *Nano Lett.* **2007**, *7* (3), 690–696. https://doi.org/10.1021/nl062795z.

(8) Li, M.; Cushing, S. K.; Wu, N. Plasmon-Enhanced Optical Sensors: A Review. *Analyst* **2015**, *140* (2), 386–406. https://doi.org/10.1039/C4AN01079E.

(9) Sanders, S.; Manjavacas, A. Analysis of the Limits of the Local Density of Photonic States near Nanostructures. *ACS Photonics* **2018**, *5* (6), 2437–2445. https://doi.org/10.1021/acsphotonics.8b00225.

(10) Della Ventura, B.; Gelzo, M.; Battista, E.; Alabastri, A.; Schirato, A.; Castaldo, G.; Corso, G.; Gentile, F.; Velotta, R. Biosensor for Point-of-Care Analysis of Immunoglobulins in Urine by Metal Enhanced Fluorescence from Gold Nanoparticles. *ACS Appl. Mater. Interfaces* **2019**, *11* (4), 3753–3762. https://doi.org/10.1021/acsami.8b20501.

(11) Bhaskar, S.; Kowshik, N. C. S. S.; Chandran, S. P.; Ramamurthy, S. S. Femtomolar Detection of Spermidine Using Au Decorated SiO2 Nanohybrid on Plasmon-Coupled Extended Cavity Nanointerface: A Smartphone-Based Fluorescence Dequenching Approach. *Langmuir* **2020**, *36* (11), 2865–2876. https://doi.org/10.1021/acs.langmuir.9b03869.

(12) Bhaskar, S.; Das, P.; Srinivasan, V.; Bhaktha B. N., S.; Ramamurthy, S. S. Plasmonic-Silver Sorets and Dielectric-Nd2O3 Nanorods for Ultrasensitive Photonic Crystal-Coupled

Emission. *Mater. Res. Bull.* **2021**, 111558. https://doi.org/10.1016/j.materresbull.2021.111558.

(13) Camposeo, A.; Persano, L.; Manco, R.; Wang, Y.; Del Carro, P.; Zhang, C.; Li, Z. Y.; Pisignano, D.; Xia, Y. Metal-Enhanced Near-Infrared Fluorescence by Micropatterned Gold Nanocages. *ACS Nano* **2015**, *9* (10), 10047–10054. https://doi.org/10.1021/acsnano.5b03624.

(14) Xie, K. X.; Liu, Q.; Jia, S. S.; Xiao, X. X. Fluorescence Enhancement by Hollow Plasmonic Assembly and Its Biosensing Application. *Anal. Chim. Acta* **2021**, *1144*, 96–101. https://doi.org/10.1016/j.aca.2020.12.008.

(15) Du, B.; Tang, C.; Zhao, D.; Zhang, H.; Yu, D.; Yu, M.; Balram, K. C.; Gersen, H.; Yang, B.; Cao, W.; Gu, C.; Besenbacher, F.; Li, J.; Sun, Y. Diameter-Optimized High-Order Waveguide Nanorods for Fluorescence Enhancement Applied in Ultrasensitive Bioassays. *Nanoscale* **2019**, *11* (30), 14322–14329. https://doi.org/10.1039/C9NR02330E.

(16) Luan, J.; Morrissey, J. J.; Wang, Z.; Derami, H. G.; Liu, K.-K.; Cao, S.; Jiang, Q.; Wang, C.; Kharasch, E. D.; Naik, R. R.; Singamaneni, S. Add-on Plasmonic Patch as a Universal Fluorescence Enhancer. *Light Sci. Appl.* **2018**, *7* (1), 29. https://doi.org/10.1038/s41377-018-0027-8.

(17) Zang, F.; Su, Z.; Zhou, L.; Konduru, K.; Kaplan, G.; Chou, S. Y. Ultrasensitive Ebola Virus Antigen Sensing via 3D Nanoantenna Arrays. *Adv. Mater.* **2019**, *31* (30), 1902331. https://doi.org/10.1002/adma.201902331.

(18) Moronshing, M.; Subramaniam, C. Room Temperature, Multiphasic Detection of Explosives, and Volatile Organic Compounds Using Thermodiffusion Driven Soret Colloids. *ACS Sustain. Chem. Eng.* **2018**, *6* (7), 9470–9479.

https://doi.org/10.1021/acssuschemeng.8b02050.

(19) Bhaskar, S.; Das, P.; Moronshing, M.; Rai, A.; Subramaniam, C.; Bhaktha, S. B. N.; Ramamurthy, S. S. Photoplasmonic Assembly of Dielectric-Metal, Nd 2 O 3 -Gold Soret Nanointerfaces for Dequenching the Luminophore Emission. *Nanophotonics* **2021**, *0* (0), 1–15. https://doi.org/10.1515/nanoph-2021-0124.

(20) Bhaskar, S.; Jha, P.; Subramaniam, C.; Ramamurthy, S. S. Multifunctional Hybrid Soret Nanoarchitectures for Mobile Phone-Based Picomolar Cu2+ Ion Sensing and Dye Degradation Applications. *Phys. E Low-Dimensional Syst. Nanostructures* **2021**, *132* (February), 114764. https://doi.org/10.1016/j.physe.2021.114764.

(21) Kelf, T. A.; Sugawara, Y.; Cole, R. M.; Baumberg, J. J.; Abdelsalam, M. E.; Cintra, S.; Mahajan, S.; Russell, A. E.; Bartlett, P. N. Localized and Delocalized Plasmons in Metallic Nanovoids. *Phys. Rev. B - Condens. Matter Mater. Phys.* **2006**, *74* (24), 245415. https://doi.org/10.1103/PhysRevB.74.245415.

(22) Bhaskar, S.; Moronshing, M.; Srinivasan, V.; Badiya, P. K.; Subramaniam, C.; Ramamurthy, S. S. Silver Soret Nanoparticles for Femtomolar Sensing of Glutathione in a Surface Plasmon-Coupled Emission Platform. *ACS Appl. Nano Mater.* **2020**, *3* (5), 4329–4341. https://doi.org/10.1021/acsanm.0c00470.

(23) Zhou, L.; Ding, F.; Chen, H.; Ding, W.; Zhang, W.; Chou, S. Y. Enhancement of Immunoassay's Fluorescence and Detection Sensitivity Using Three-Dimensional Plasmonic Nano-Antenna-Dots Array. *Anal. Chem.* **2012**, *84* (10), 4489–4495. https://doi.org/10.1021/ac3003215.

(24) Flauraud, V.; Regmi, R.; Winkler, P. M.; Alexander, D. T. L.; Rigneault, H.; van Hulst, N. F.; García-Parajo, M. F.; Wenger, J.; Brugger, J. In-Plane Plasmonic Antenna Arrays with

Surface Nanogaps for Giant Fluorescence Enhancement. *Nano Lett.* **2017**, *17* (3), 1703–1710. https://doi.org/10.1021/acs.nanolett.6b04978.

(25) Kinkhabwala, A.; Yu, Z.; Fan, S.; Avlasevich, Y.; Müllen, K.; Moerner, W. E. Large Single-Molecule Fluorescence Enhancements Produced by a Bowtie Nanoantenna. *Nat. Photonics* **2009**, *3* (11), 654–657. https://doi.org/10.1038/nphoton.2009.187.

(26) Puchkova, A.; Vietz, C.; Pibiri, E.; Wünsch, B.; Sanz Paz, M.; Acuna, G. P.; Tinnefeld, P. DNA Origami Nanoantennas with over 5000-Fold Fluorescence Enhancement and Single-Molecule Detection at 25 MM. *Nano Lett.* **2015**, *15* (12), 8354–8359. https://doi.org/10.1021/acs.nanolett.5b04045.

(27) Jeong, Y.; Kook, Y.-M.; Lee, K.; Koh, W.-G. Metal Enhanced Fluorescence (MEF) for Biosensors: General Approaches and a Review of Recent Developments. *Biosens. Bioelectron.* **2018**, *111* (March), 102–116. https://doi.org/10.1016/j.bios.2018.04.007.

(28) Mayer, K. M.; Hafner, J. H. Localized Surface Plasmon Resonance Sensors. *Chem. Rev.* **2011**, *111* (6), 3828–3857. https://doi.org/10.1021/cr100313v.

(29) Kaye, S.; Zeng, Z.; Sanders, M.; Chittur, K.; Koelle, P. M.; Lindquist, R.; Manne, U.; Lin, Y.; Wei, J. Label-Free Detection of DNA Hybridization with a Compact LSPR-Based Fiber-Optic Sensor. *Analyst* **2017**, *142* (11), 1974–1981. https://doi.org/10.1039/c7an00249a.

(30) Kawasaki, D.; Yamada, H.; Maeno, K.; Sueyoshi, K.; Hisamoto, H.; Endo, T. Core-Shell-Structured Gold Nanocone Array for Label-Free DNA Sensing. *ACS Appl. Nano Mater.* **2019**, *2* (8), 4983–4990. https://doi.org/10.1021/acsanm.9b00930.

(31) Minopoli, A.; Scardapane, E.; Acunzo, A.; Campanile, R.; Della Ventura, B.; Velotta, R. Analysis of the Optical Response of a SARS-CoV-2-Directed Colorimetric Immunosensor. *AIP Adv.* **2021**, *11* (6), 065319. https://doi.org/10.1063/5.0050570.

(32) Loza, K.; Diendorf, J.; Sengstock, C.; Ruiz-Gonzalez, L.; Gonzalez-Calbet, J. M.; Vallet-Regi, M.; Köller, M.; Epple, M. The Dissolution and Biological Effects of Silver Nanoparticles in Biological Media. *J. Mater. Chem. B* **2014**, *2* (12), 1634–1643. https://doi.org/10.1039/c3tb21569e.

(33) Zhang, X. Gold Nanoparticles: Recent Advances in the Biomedical Applications. *Cell Biochem. Biophys.* **2015**, *72* (3), 771–775. https://doi.org/10.1007/s12013-015-0529-4.

(34) Minopoli, A.; Sakač, N.; Lenyk, B.; Campanile, R.; Mayer, D.; Offenhäusser, A.; Velotta, R.; Della Ventura, B. LSPR-Based Colorimetric Immunosensor for Rapid and Sensitive 17β-Estradiol Detection in Tap Water. *Sensors Actuators B Chem.* **2020**, *308*, 127699. https://doi.org/10.1016/j.snb.2020.127699.

(35) Bhaskar, S.; Visweswar Kambhampati, N. S.; Ganesh, K. M.; P, M. S.; Srinivasan, V.; Ramamurthy, S. S. Metal-Free, Graphene Oxide-Based Tunable Soliton and Plasmon Engineering for Biosensing Applications. *ACS Appl. Mater. Interfaces* **2021**, *13* (14), 17046–17061. https://doi.org/10.1021/acsami.1c01024.

(36) Wang, J.; Le-The, H.; Karamanos, T.; Suryadharma, R. N. S.; van den Berg, A.; Pinkse, P. W. H.; Rockstuhl, C.; Shui, L.; Eijkel, J. C. T.; Segerink, L. I. Plasmonic Nanocrystal Arrays on Photonic Crystals with Tailored Optical Resonances. *ACS Appl. Mater. Interfaces* **2020**, *12* (33), 37657–37669. https://doi.org/10.1021/acsami.0c05596.

(37) Chen, G.; Wang, D.; Hong, W.; Sun, L.; Zhu, Y.; Chen, X. Fluorescence Enhancement on Large Area Self-Assembled Plasmonic-3D Photonic Crystals. *Small* **2017**, *13* (9), 1602612. https://doi.org/10.1002/smll.201602612.

(38) Lee, W.; Lee, S. Y.; Briber, R. M.; Rabin, O. Self-Assembled SERS Substrates with Tunable Surface Plasmon Resonances. *Adv. Funct. Mater.* **2011**, *21* (18), 3424–3429.

https://doi.org/10.1002/adfm.201101218.

(39) Jang, Y. H.; Chung, K.; Quan, L. N.; Špačková, B.; Šípová, H.; Moon, S.; Cho, W. J.; Shin, H. Y.; Jang, Y. J.; Lee, J. E.; Kochuveedu, S. T.; Yoon, M. J.; Kim, J.; Yoon, S.; Kim, J. K.; Kim, D.; Homola, J.; Kim, D. H. Configuration-Controlled Au Nanocluster Arrays on Inverse Micelle Nano-Patterns: Versatile Platforms for SERS and SPR Sensors. *Nanoscale* **2013**, *5* (24), 12261–12271. https://doi.org/10.1039/c3nr03860b.

(40) Kasani, S.; Curtin, K.; Wu, N. A Review of 2D and 3D Plasmonic Nanostructure Array Patterns: Fabrication, Light Management and Sensing Applications. *Nanophotonics* **2019**, *8* (12), 2065–2089. https://doi.org/10.1515/nanoph-2019-0158.

(41) Ghosh, S. K.; Pal, T. Interparticle Coupling Effect on the Surface Plasmon Resonance of Gold Nanoparticles: From Theory to Applications. *Chem. Rev.* **2007**, *107* (11), 4797–4862. https://doi.org/10.1021/cr0680282.

(42) Nordlander, P.; Oubre, C.; Prodan, E.; Li, K.; Stockman, M. I. Plasmon Hybridization in Nanoparticle Dimers. *Nano Lett.* **2004**, *4* (5), 899–903. https://doi.org/10.1021/nl049681c.

(43) Sheikholeslami, S.; Jun, Y. W.; Jain, P. K.; Alivisatos, A. P. Coupling of Optical Resonances in a Compositionally Asymmetric Plasmonic Nanoparticle Dimer. *Nano Lett.* **2010**, *10* (7), 2655–2660. https://doi.org/10.1021/nl101380f.

(44) Masterson, A. N.; Liyanage, T.; Kaimakliotis, H.; Gholami Derami, H.; Deiss, F.; Sardar, R. Bottom-Up Fabrication of Plasmonic Nanoantenna-Based High-Throughput Multiplexing Biosensors for Ultrasensitive Detection of MicroRNAs Directly from Cancer Patients' Plasma. *Anal. Chem.* **2020**, *92* (13), 9295–9304. https://doi.org/10.1021/acs.analchem.0c01639.

(45) Liao, Z.; Zhang, Y.; Li, Y.; Miao, Y.; Gao, S.; Lin, F.; Deng, Y.; Geng, L. Microfluidic

Chip Coupled with Optical Biosensors for Simultaneous Detection of Multiple Analytes: A Review. *Biosens. Bioelectron.* **2019**, *126* (August 2018), 697–706. https://doi.org/10.1016/j.bios.2018.11.032.

(46) Rajeeva, B. B.; Lin, L.; Zheng, Y. Design and Applications of Lattice Plasmon Resonances. *Nano Res.* **2018**, *11* (9), 4423–4440. https://doi.org/10.1007/s12274-017-1909-4.

(47) Kravets, V. G.; Kabashin, A. V.; Barnes, W. L.; Grigorenko, A. N. Plasmonic Surface Lattice Resonances: A Review of Properties and Applications. *Chemical Reviews*. 2018, pp 5912–5951. https://doi.org/10.1021/acs.chemrev.8b00243.

(48) Kraus, T.; Malaquin, L.; Schmid, H.; Riess, W.; Spencer, N. D.; Wolf, H. Nanoparticle Printing with Single-Particle Resolution. *Nat. Nanotechnol.* **2007**, *2* (9), 570–576. https://doi.org/10.1038/nnano.2007.262.

(49) Yin, Y.; Lu, Y.; Gates, B.; Xia, Y. Template-Assisted Self-Assembly: A Practical Route to Complex Aggregates of Monodispersed Colloids with Well-Defined Sizes, Shapes, and Structures. *J. Am. Chem. Soc.* **2001**, *123* (36), 8718–8729. https://doi.org/10.1021/ja011048v.

(50) Cheung, C. L.; Nikolić, R. J.; Reinhardt, C. E.; Wang, T. F. Fabrication of Nanopillars by Nanosphere Lithography. *Nanotechnology* **2006**, *17* (5), 1339–1343. https://doi.org/10.1088/0957-4484/17/5/028.

(51) Glass, R.; M ller, M.; Spatz, J. P. Block Copolymer Micelle Nanolithography. *Nanotechnology* **2003**, *14* (10), 1153–1160. https://doi.org/10.1088/0957-4484/14/10/314.

(52) Minopoli, A.; Della Ventura, B.; Lenyk, B.; Gentile, F.; Tanner, J. A.; Offenhäusser, A.; Mayer, D.; Velotta, R. Ultrasensitive Antibody-Aptamer Plasmonic Biosensor for Malaria Biomarker Detection in Whole Blood. *Nat. Commun.* **2020**, *11* (1), 6134.

https://doi.org/10.1038/s41467-020-19755-0.

(53) Minopoli, A.; Della Ventura, B.; Campanile, R.; Tanner, J. A.; Offenhäusser, A.; Mayer, D.; Velotta, R. Randomly Positioned Gold Nanoparticles as Fluorescence Enhancers in Apta-Immunosensor for Malaria Test. *Microchim. Acta* **2021**, *188* (3), 88. https://doi.org/10.1007/s00604-021-04746-9.

(54) Snow, R. W. Global Malaria Eradication and the Importance of Plasmodium Falciparum Epidemiology in Africa. *BMC Med.* **2015**, *13* (1), 23. https://doi.org/10.1186/s12916-014-0254-7.

(55) Funari, R.; Della Ventura, B.; Altucci, C.; Offenhäusser, A.; Mayer, D.; Velotta, R. Single Molecule Characterization of UV-Activated Antibodies on Gold by Atomic Force Microscopy. *Langmuir* **2016**, *32* (32), 8084–8091. https://doi.org/10.1021/acs.langmuir.6b02218.

(56) Della Ventura, B.; Banchelli, M.; Funari, R.; Illiano, A.; De Angelis, M.; Taroni, P.; Amoresano, A.; Matteini, P.; Velotta, R. Biosensor Surface Functionalization by a Simple Photochemical Immobilization of Antibodies: Experimental Characterization by Mass Spectrometry and Surface Enhanced Raman Spectroscopy. *Analyst* **2019**, *144* (23), 6871–6880. https://doi.org/10.1039/C9AN00443B.

(57) Jiang, C.; Markutsya, S.; Tsukruk, V. V. Collective and Individual Plasmon Resonances in Nanoparticle Films Obtained by Spin-Assisted Layer-by-Layer Assembly. *Langmuir* **2004**, *20* (3), 882–890. https://doi.org/10.1021/la0355085.

(58) Jenkins, J. A.; Zhou, Y.; Thota, S.; Tian, X.; Zhao, X.; Zou, S.; Zhao, J. Blue-Shifted Narrow Localized Surface Plasmon Resonance from Dipole Coupling in Gold Nanoparticle Random Arrays. *J. Phys. Chem. C* **2014**, *118* (45), 26276–26283.

https://doi.org/10.1021/jp508181g.

(59) Della Ventura, B.; Iannaccone, M.; Funari, R.; Pica Ciamarra, M.; Altucci, C.; Capparelli, R.; Roperto, S.; Velotta, R. Effective Antibodies Immobilization and Functionalized Nanoparticles in a Quartz-Crystal Microbalance-Based Immunosensor for the Detection of Parathion. *PLoS One* **2017**, *12* (2), e0171754. https://doi.org/10.1371/journal.pone.0171754.

(60) Goutelle, S.; Maurin, M.; Rougier, F.; Barbaut, X.; Bourguignon, L.; Ducher, M.; Maire, P. The Hill Equation: A Review of Its Capabilities in Pharmacological Modelling. *Fundam. Clin. Pharmacol.* **2008**, *22* (6), 633–648. https://doi.org/10.1111/j.1472-8206.2008.00633.x.

(61) Li, Y.; Wang, Y.; Huang, G.; Gao, J. Cooperativity Principles in Self-Assembled Nanomedicine. *Chem. Rev.* **2018**, acs.chemrev.8b00195. https://doi.org/10.1021/acs.chemrev.8b00195.

(62) Xie, K.-X.; Liu, Q.; Song, X.-L.; Huo, R.-P.; Shi, X.-H.; Liu, Q.-L. Amplified Fluorescence by Hollow-Porous Plasmonic Assembly: A New Observation and Its Application in Multiwavelength Simultaneous Detection. *Anal. Chem.* **2021**, *93* (8), 3671–3676. https://doi.org/10.1021/acs.analchem.0c05219.

(63) Luo, X.; Zhao, X.; Wallace, G. Q.; Brunet, M. H.; Wilkinson, K. J.; Wu, P.; Cai, C.; Bazuin, C. G.; Masson, J. F. Multiplexed SERS Detection of Microcystins with Aptamer-Driven Core-Satellite Assemblies. *ACS Appl. Mater. Interfaces* **2021**, *13* (5), 6545–6556. https://doi.org/10.1021/acsami.0c21493.

(64) Fossati, S.; Hageneder, S.; Menad, S.; Maillart, E.; Dostalek, J. Multiresonant Plasmonic Nanostructure for Ultrasensitive Fluorescence Biosensing. *Nanophotonics* **2020**, *9* (11),

3673–3685. https://doi.org/10.1515/nanoph-2020-0270.

(65) Tang, B.; Wang, J.; Hutchison, J. A.; Ma, L.; Zhang, N.; Guo, H.; Hu, Z.; Li, M.; Zhao, Y. Ultrasensitive, Multiplex Raman Frequency Shift Immunoassay of Liver Cancer Biomarkers in Physiological Media. *ACS Nano* **2016**, *10* (1), 871–879. https://doi.org/10.1021/acsnano.5b06007.

(66) Orlov, A. V.; Pushkarev, A. V.; Znoyko, S. L.; Novichikhin, D. O.; Bragina, V. A.; Gorshkov, B. G.; Nikitin, P. I. Multiplex Label-Free Biosensor for Detection of Autoantibodies in Human Serum: Tool for New Kinetics-Based Diagnostics of Autoimmune Diseases. *Biosens. Bioelectron.* **2020**, *159* (April), 112187. https://doi.org/10.1016/j.bios.2020.112187.

(67) Li, L.; Pan, L.; Ma, Z.; Yan, K.; Cheng, W.; Shi, Y.; Yu, G. All Inkjet-Printed Amperometric Multiplexed Biosensors Based on Nanostructured Conductive Hydrogel Electrodes. *Nano Lett.* **2018**, *18* (6), 3322–3327. https://doi.org/10.1021/acs.nanolett.8b00003.

(68) Eissa, S.; Zourob, M. Ultrasensitive Peptide-Based Multiplexed Electrochemical Biosensor for the Simultaneous Detection of Listeria Monocytogenes and Staphylococcus Aureus. *Microchim. Acta* **2020**, *187* (9), 486. https://doi.org/10.1007/s00604-020-04423-3.

(69) Turgut-Balik, D.; Akbulut, E.; Shoemark, D. K.; Celik, V.; Moreton, K. M.; Sessions, R. B.; Holbrook, J. J.; Brady, R. L. Cloning, Sequence and Expression of the Lactate Dehydrogenase Gene from the Human Malaria Parasite, Plasmodium Vivax. *Biotechnol. Lett.* **2004**, *26* (13), 1051–1055. https://doi.org/10.1023/B:BILE.0000032958.78158.10.

(70) Cheung, Y.-W.; Dirkzwager, R. M.; Wong, W.-C.; Cardoso, J.; D'Arc Neves Costa, J.; Tanner, J. A. Aptamer-Mediated Plasmodium-Specific Diagnosis of Malaria. *Biochimie* **2018**, *145*, 131–136. https://doi.org/10.1016/j.biochi.2017.10.017.

(71) Guzatov, D. V.; Vaschenko, S. V.; Stankevich, V. V.; Lunevich, A. Y.; Glukhov, Y. F.; Gaponenko, S. V. Plasmonic Enhancement of Molecular Fluorescence near Silver Nanoparticles: Theory, Modeling, and Experiment. *J. Phys. Chem. C* **2012**, *116* (19), 10723–10733. https://doi.org/10.1021/jp301598w.

(72) Chen, H.; Wang, X.; Li, J.; Wang, X. Cotton Derived Carbonaceous Aerogels for the Efficient Removal of Organic Pollutants and Heavy Metal Ions. *J. Mater. Chem. A* **2015**, *3* (11), 6073–6081. https://doi.org/10.1039/c5ta00299k.

(73) Prodan, E.; Nordlander, P. Plasmon Hybridization in Spherical Nanoparticles. *J. Chem. Phys.* **2004**, *120* (11), 5444–5454. https://doi.org/10.1063/1.1647518.

(74) Huang, Y.; Chen, Y.; Wang, L. L.; Ringe, E. Small Morphology Variations Effects on Plasmonic Nanoparticle Dimer Hotspots. *J. Mater. Chem. C* **2018**, *6* (36), 9607–9614. https://doi.org/10.1039/C8TC03556C.

(75) Montaño-Priede, J. L.; Pal, U. Estimating Near Electric Field of Polyhedral Gold Nanoparticles for Plasmon-Enhanced Spectroscopies. *J. Phys. Chem. C* **2019**, *123* (18), 11833–11839. https://doi.org/10.1021/acs.jpcc.9b01105.

(76) Povedailo, V. A.; Lysenko, I. L.; Tikhomirov, S. A.; Yakovlev, D. L.; Tsybulsky, D. A.; Kruhlik, A. S.; Fan, F.; Martynenko-Makaev, Y. V.; Sharko, O. L.; Duong, P. V.; Minh, P. H.; Shmanai, V. V. Fluorescent Properties of Carboxyfluorescein Bifluorophores. *J. Fluoresc.* **2020**, *30* (3), 629–635. https://doi.org/10.1007/s10895-020-02535-w.

(77) Mujumdar, R. B.; Ernst, L. A.; Mujumdar, S. R.; Lewis, C. J.; Waggoner, A. S. Cyanine Dye Labeling Reagents: Sulfoindocyanine Succinimidyl Esters. *Bioconjug. Chem.* **1993**, *4* (2), 105–111. https://doi.org/10.1021/bc00020a001.

(78) Le Ru, E. C.; Blackie, E.; Meyer, M.; Etchegoint, P. G. Surface Enhanced Raman Scattering

Enhancement Factors: A Comprehensive Study. *J. Phys. Chem. C* **2007**, *111* (37), 13794–13803. https://doi.org/10.1021/jp0687908.

(79) Neves-Petersen, M. T.; Gryczynski, Z.; Lakowicz, J.; Fojan, P.; Pedersen, S.; Petersen, E.; Bjørn Petersen, S. High Probability of Disrupting a Disulphide Bridge Mediated by an Endogenous Excited Tryptophan Residue. *Protein Sci.* **2009**, *11* (3), 588–600. https://doi.org/10.1110/ps.06002.

(80) Ioerger, T. R.; Du, C.; Linthicum, D. S. Conservation of Cys–Cys Trp Structural Triads and Their Geometry in the Protein Domains of Immunoglobulin Superfamily Members. *Mol. Immunol.* **1999**, *36* (6), 373–386. https://doi.org/10.1016/S0161-5890(99)00032-2.

(81) Neves-Petersen, M. T.; Klitgaard, S.; Pascher, T.; Skovsen, E.; Polivka, T.; Yartsev, A.; Sundström, V.; Petersen, S. B. Flash Photolysis of Cutinase: Identification and Decay Kinetics of Transient Intermediates Formed upon UV Excitation of Aromatic Residues. *Biophys. J.* **2009**, *97* (1), 211–226. https://doi.org/10.1016/j.bpj.2009.01.065.

FOR TABLE OF CONTENTS ONLY